LETTER | MAY 25 2022

Piezo-optomechanical cantilever modulators for VLSI visible photonics

Mark Dong; David Heim; Alex Witte; ... et. al

APL Photonics 7, 051304 (2022)
https://doi.org/10.1063/5.0088424

Piezo-optomechanical cantilever modulators for VLSI visible photonics

Cite as: APL Photon. 7, 051304 (2022); doi: 10.1063/5.0088424
Submitted: 16 February 2022 • Accepted: 30 March 2022 •
Published Online: 25 May 2022

Mark Dong,[1,2,a] David Heim,[1] Alex Witte,[1] Genevieve Clark,[1,2] Andrew J. Leenheer,[3] Daniel Dominguez,[3] Matthew Zimmermann,[1] Y. Henry Wen,[1] Gerald Gilbert,[4,a] Dirk Englund,[2,5,a] and Matt Eichenfield[3,a]

AFFILIATIONS

[1] The MITRE Corporation, 202 Burlington Road, Bedford, Massachusetts 01730, USA
[2] Research Laboratory of Electronics, Massachusetts Institute of Technology, Cambridge, Massachusetts 02139, USA
[3] Sandia National Laboratories, P.O. Box 5800, Albuquerque, New Mexico 87185, USA
[4] The MITRE Corporation, 200 Forrestal Road, Princeton, New Jersey 08540, USA
[5] Brookhaven National Laboratory, 98 Rochester St., Upton, New York 11973, USA

[a] **Authors to whom correspondence should be addressed:** mdong@mitre.org; ggilbert@mitre.org; englund@mit.edu; and meichen@sandia.gov

ABSTRACT

Visible-wavelength very large-scale integration photonic circuits have a potential to play important roles in quantum information and sensing technologies. The realization of scalable, high-speed, and low-loss photonic mesh circuits depends on reliable and well-engineered visible photonic components. Here, we report a low-voltage optical phase shifter based on piezo-actuated mechanical cantilevers, fabricated on a CMOS compatible, 200 mm wafer-based visible photonics platform. We show linear phase and amplitude modulation with 6 V_π cm in differential operation, −1.5 to −2 dB insertion loss, and up to 40 dB contrast in the 700–780 nm range. By adjusting selected cantilever parameters, we demonstrate a low-displacement and a high-displacement device, both exhibiting a nearly flat frequency response from DC to a peak mechanical resonance at 23 and 6.8 MHz respectively, which, through resonant enhancement of Q ~ 40, further decreases the operating voltage down to 0.15 V_π cm.

I. INTRODUCTION

There is currently an increasing demand for very large-scale integration (VLSI) photonic circuits[1,2] that provide precise, rapid, and low-power control of visible optical fields. Quantum information applications from quantum computing and networks to sensing[3–5] increasingly rely on atom[6–8] and atom-like[9–11] systems, which make use of optical transitions in the visible wavelength regime. In chemical sensing and imaging, visible light is required to interact with particular molecular species[12] and to achieve higher resolution than possible with longer wavelengths. A leading approach for large-scale optical control is programmable Mach–Zehnder meshes (MZMs),[1] built from cascaded Mach–Zehnder interferometers (MZIs) [Fig. 1(a)]. Each MZI performs the unitary operation $U(2)$ as the fundamental building block for different types of meshes,[13–16] such as multi-port interferometers [Fig. 1(b)] and binary trees [Fig. 1(c)]. The complexity of scaling these circuits requires high-quality individual MZIs and has led to the development of many modulation schemes. In the near-infrared (NIR), phase modulation in MZIs has been demonstrated at large-scale with thermo-optic phase shifters[17–21] and in individual devices using free-carriers,[22] $\chi^{(2)}$ nonlinearities,[23–25] and MEMS.[26] In the visible regime, previous reports on thermo-optic[27–29] and thin-film lithium niobate[30] MZIs show promise for VLSI photonics, but there remains an open challenge to build reliable MZMs that satisfy application requirements of high switching bandwidths (>10 MHz), high contrasts (>40 dB), and low losses (<1 dB) per modulator.

To address this need, we previously introduced a programmable MZM platform[31] based on visible-spectrum silicon nitride (SiN_x) waveguides with high-speed (>100 MHz) aluminum nitride (AlN) piezo-modulation.[32] However, the modulators in this mesh have a high voltage-loss product (175 V dB), defined as VLP = $V_\pi \times \alpha_m$, where V_π is the voltage required for a π-phase shift and α_m is the modulator insertion loss. The VLP metric governs the

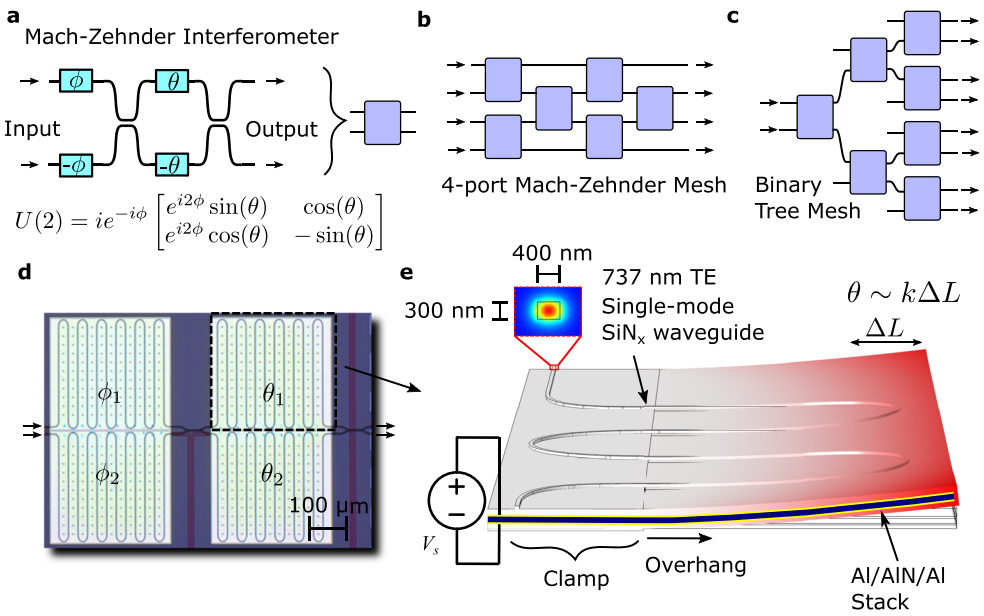

FIG. 1. Piezo-optomechanical cantilevers for large-scale visible photonics: (a) diagram of a Mach–Zehnder interferometer with four phase shifters in push–pull configuration performing the $U(2)$ operation; (b) schematic of a 4-port Mach–Zehnder mesh; (c) schematic of a 2 × 8 binary tree mesh; (d) optical microscope image of a fabricated device with four integrated cantilever phase shifters, each controlling the phases $\theta_{1,2}$, $\phi_{1,2}$; (e) operating principles of a piezo-optomechanical cantilever phase shifter, showing that an applied voltage V_s across an aluminum nitride piezo imparts a path-length change to the integrated SiN_x waveguides, inducing an effective phase shift θ.

limit on possible mesh circuit depths, given the maximum voltage (e.g., set by CMOS driver circuitry) and optical loss requirements. Conversely, for a set mesh size, cascading high-VLP modulators to reduce V_π or improve unitary fidelity[33] may not be possible due to increasing photon losses. As the number of optical components in a mesh generally increases quadratically with the number of input/output fields,[15] modulators with low VLPs are highly desirable.

In this work, we demonstrate a visible-spectrum phase and amplitude modulator using piezo-actuated mechanical cantilevers. An improved undercut process in the fabrication enables reliable, singly clamped cantilevers with large released regions (>500 μm) and lower VLPs in the 20–30 V dB range, an order of magnitude improvement over our previous work.[31,34] The optically broadband modulator has a 6 V_π cm, up to >40 dB extinction, low hold-power consumption (<30 nW), −1.5 to −2 dB insertion loss, and minimal modulation losses. Moreover, the modulator exhibits a nearly flat frequency response from DC to a peak mechanical eigenmode (up to tens of MHz) for nanosecond switching or resonantly enhanced actuation to further reduce operating voltage (down to 0.15 V_π cm or 0.8 V dB). We arrange the phase modulators for differential operation[13] in an MZI configuration [microscope image shown in Fig. 1(d)] with the four possible phase shifts labeled. The device consists of 400 nm wide × 300 nm thick SiN_x waveguides coupled to an AlN piezo-stack [Fig. 1(e)]. The modulator operates by applying a voltage V_s across the piezo-layer, which mechanically deforms the cantilever and induces a path length change ΔL and phase shift θ in the waveguides. We characterize the device across the 700–780 nm wavelength range and explore different cantilever designs to target various operating regimes.

II. PHASE SHIFTER FABRICATION AND DESIGN

We illustrate the cantilever design in Fig. 2. A scanning electron microscope (SEM) image is shown in Fig. 2(a) of the fully fabricated and released cantilever with false-colored SiN_x waveguides, which are looped several times across the surface of the cantilever to increase the phase shifter response. Figure 2(b) maps out a cross section of our entire layer stack.

The fabrication is based on a 200 mm-wafer optical lithography process at Sandia National Labs, which we briefly summarize. First, a bottom aluminum metal layer (M1) is patterned and etched for routing electrical signals and grounds. We then deposit and pattern a sacrificial amorphous-Si (a-Si) layer for defining the cantilevers. Next, a stack of aluminum, aluminum nitride, aluminum (Al/AlN/Al) forms the electrodes and piezo-layers for optomechanical actuation. After some buffer oxide, we deposit and etch the SiN_x waveguides to form the optical waveguides. We next etch a set of small release holes through the entire stack [Fig. 2(b)], exposing additional a-Si to facilitate device release. Finally, post wafer dicing, a xenon difluoride (XeF_2) process removes the a-Si, undercutting all cantilever devices on a single die.

The physical mechanisms that contribute to the optical phase shift is primarily due to waveguide path length deformations induced by applying voltages across the piezo-layer, in addition to stress-optic effects.[35] Using finite-element models (COMSOL

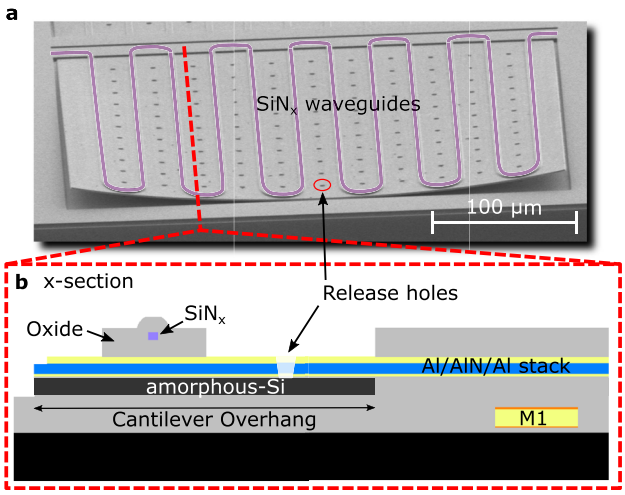

FIG. 2. Basic design and layer stack of a piezo-optomechanical cantilever phase shifter: (a) SEM of a 300 μm overhang length cantilever with SiN_x waveguides colored purple; (b) cross section schematic of a cantilever, depicting the cantilever overhang defined by the sacrificial amorphous-Si layer, SiN_x waveguide (purple) and oxide cladding (gray), aluminum (yellow)/aluminum nitride (blue) piezo-stack, and the aluminum routing metal M1. Etched release holes are shown to enable removal of the amorphous-Si layer for large overhangs.

Multiphysics®) of our cantilever geometry, we calculate the displacement tensor $\nabla\mathbf{u}$, defined as the gradient of the mechanical displacement vector field $\mathbf{u}$, for a given applied voltage V_s. Integrating the displacement tensor along the meandering waveguide path [Fig. 2(a)], which we define as a curve C, we find the path length change ΔL to be

$$\Delta L = \int_C ds\, \hat{s} \cdot \nabla\mathbf{u} \cdot \hat{s}, \tag{1}$$

where $\hat{s}$ is the unit vector parallel to the path C. This length deformation then induces a phase shift

$$\theta = 2\pi n_{eff} \Delta L/\lambda, \tag{2}$$

where $n_{eff} = 1.68$ is the effective modal index of our waveguide. Based on our simulations, for an $h = 30$ μm overhang cantilever at $V_s = 10$ V, we estimate a total $\Delta L = 0.89$ nm for a single waveguide loop, corresponding to $\theta \sim 0.004\pi$ radians at 737 nm wavelength. We note that at lower wavelengths, the phase-shifter becomes more effective, ultimately limited by the transparency window of our SiN_x. We also find in the linear elastic regime (applicable for the small strain values present in our system) that ΔL scales approximately linearly with cantilever overhang h and the number of waveguide loops N_L.

The induced phase shift's dependence on the cantilever and waveguide geometric parameters h and N_L allows for a trade-off between device size, operating voltage, optical losses, and mechanical resonance frequency. Accordingly, we design two different cantilever geometries: design 1 is a high-displacement cantilever, optimized for DC, low voltage operation with a lower peak mechanical frequency, while design 2 is a low-displacement cantilever, optimized for AC, fast switching with a higher peak mechanical frequency. Table I summarizes the geometries and measured characteristics of the two devices based on experiments described in Sec. III.

III. DEVICE CHARACTERIZATION

We characterize our cantilever modulator's performance by measuring MZIs with both design 1 and design 2 parameters by actuating the two internal phase shifters per MZI, each contributing a phase of $\theta_{1,2}$ [Fig. 1(c)], while the additional phase shifts $\phi_{1,2}$ are unused. We use a 250-μm pitch fiber array to couple a broadly tunable continuous-wave (CW) Ti:sapphire laser into our SiN_x waveguides through on-chip gratings designed for the 700–780 nm range. DC and AC electrical signals are delivered with a ground-signal-ground (GSG) RF probe touching down onto electrical pads connected to the phase shifters for active modulation. Insertion losses measured at 737 nm wavelength typically range from −1.5 to −2 dB per modulator after subtracting the grating coupler efficiencies.

A. Design 1: DC actuation

We first characterize a design 1 MZI by applying a single voltage signal V_s connected in opposite polarities to the two phase shifters such that nominally $\theta_1 = -\theta_2$. Figure 3 shows the normalized optical transmission from the MZI's cross-port as the voltage V_s is swept from 0 to 30 V at a 0.25 V step size. We plot modulation performances across 705, 737, and 780 nm wavelengths [Fig. 3(a)] and find the V_π values via a sinusoidal fit of the data to be 14.0, 15.2, and 16.3 V, respectively, increasing with wavelength. The total SiN_x

TABLE I. Measured characteristics of piezo-optomechanical cantilevers.

Device	Overhang h (μm)	Waveguide loops N_L	Peak resonance frequency (MHz)	Footprint (μm^2)	V_π (V)	α_m (dB)	Voltage-loss product VLP (V-dB)
Design 1 cantilever (high-displacement)	300	6	6.8	350 × 325	15	−1.5	22
Design 2 cantilever (low-displacement)	80	19	23.3	100 × 650	18	−2.0	36

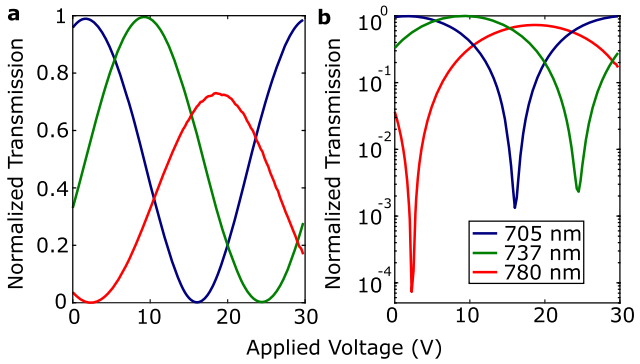

FIG. 3. DC of actuation a piezo-optomechanical modulator with design 1 parameters: (a) normalized transmission of cross-port at 705, 737, and 780 nm; (b) log scale of same data.

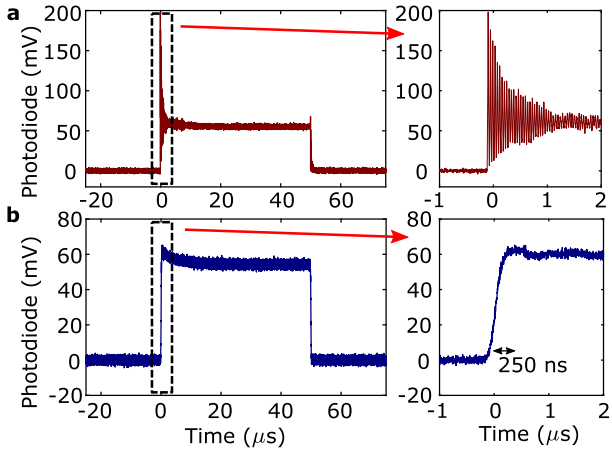

FIG. 4. Switching characteristics of a piezo-optomechanical modulator with design 2 parameters: (a) cross-port time-trace (16 averages) of an applied 10 kHz square wave showing long-lived mechanical resonances; (b) cross-port time-trace (16 averages) of an applied 10 kHz tanh square showing a smooth transition with a rise time of 250 ns.

waveguide length for design 1 is 3.9 mm (accounting for all loops), and thus, we calculate $V_\pi L$ ranging from 5.5 to 6.3 V cm. The passive directional couplers in our modulator are optimized (50:50 splitting) around 737 nm, and thus, the depth of modulation decreases as the wavelength moves farther away from this wavelength.[33] The splitting ratios, seen more clearly in log scale [Fig. 3(b)], vary by wavelength and dip below 40 dB for 780 nm, while 737 and 705 nm show 28–30 dB, respectively. We attribute the variation to differences in polarization and frequency stability of the laser at different wavelength set points.

B. Design 2: AC actuation and mechanical resonance enhancement

We next investigate a design 2 MZI to determine the temporal response and mechanical resonances present in the cantilever. For the experiments in this section, we apply an AC signal to modulate phase shifter θ_1 only, while the other phase shifter θ_2 is set to a specific DC bias point depending on the measurement.

The switching behavior of our modulator is characterized by applying various switch signals. Here, the phase θ_2 is biased such that the modulator turns "on" and "off" as θ_1 is modulated. When a simple square wave is applied [Fig. 4(a)], we observe many excited mechanical resonances, including a long-lived oscillation at ~23 MHz. The high frequency components in the sharp square edge can be suppressed by tailoring a smoothed (hyperbolic tangent) switch signal, resulting in a clean transition with a 250 ns rise time [Fig. 4(b)] more suitable for applications requiring faster time scales.

We next measure the modulator's frequency transfer function using small-signal (0.5 V pk–pk) sinusoids on θ_1 while setting θ_2 to the maximum slope of the MZI's amplitude response for enhanced contrast. Figure 5(a) plots the device's modulation amplitude as the small-signal sine is swept in frequency, normalized to the DC response. Several piezo-mechanical resonances[36] are clearly seen at 1.8, 4.4, 8.3, 14.1 MHz, and the long-lived 23.3 MHz resonance responsible for the oscillations observed in Fig. 4(a). Finite-element modeling of the cantilever confirms eigenmodes close to the measured frequencies, showing the resonances belong to the same family of modes. We show two lower order resonances at 1.8 and 4.4 MHz [Fig. 5(b)], simulated on a cantilever subsection, to illustrate the mechanical deformations. The number of ripples along the free-hanging portion of the cantilever increases for the higher frequency eigenmodes. We note that the measured resonance peaks are similar to those observed in other piezo-electronic systems.[37,38]

The presence of cantilever mechanical eigenmodes particular to each phase shifter allows for the resonances to greatly enhance the phase shift per voltage response. We focus on the peak mode at 23.3 MHz, for which the mechanical ripples and the waveguide loops are spatially aligned approximately in a 1:1 ratio. We record a time-resolved trace of the cross port output while applying sine waves at 20 MHz (off-resonance) and 23 MHz (on-resonance) to θ_1 [Fig. 5(c)]. A large enhancement (~15 dB) of the modulator response is seen due to the mechanical resonance effects. By adjusting the amplitude of the applied sine wave until the modulator output saturates, we measure the single cantilever V_π to be 0.8 V. The total SiN_x waveguide length for design 2 is 3.62 mm, corresponding to a $V_\pi L$ of 0.3 V cm (or 0.15 V cm for two cantilevers in differential operation). Comparing the resonant V_π to the static V_π of a single cantilever (36 V) for design 2 (see supplementary material), the mechanical Q is estimated to be ~40. The interaction between the optics and the mechanical resonance further contributes to the path displacement effect as well as strain-optic effects—we are currently investigating the detailed theory of the resonant piezo-optoelectronic physics.

IV. DISCUSSION

We presented two specific designs for our piezo-optomechanical modulator, highlighting its versatility and

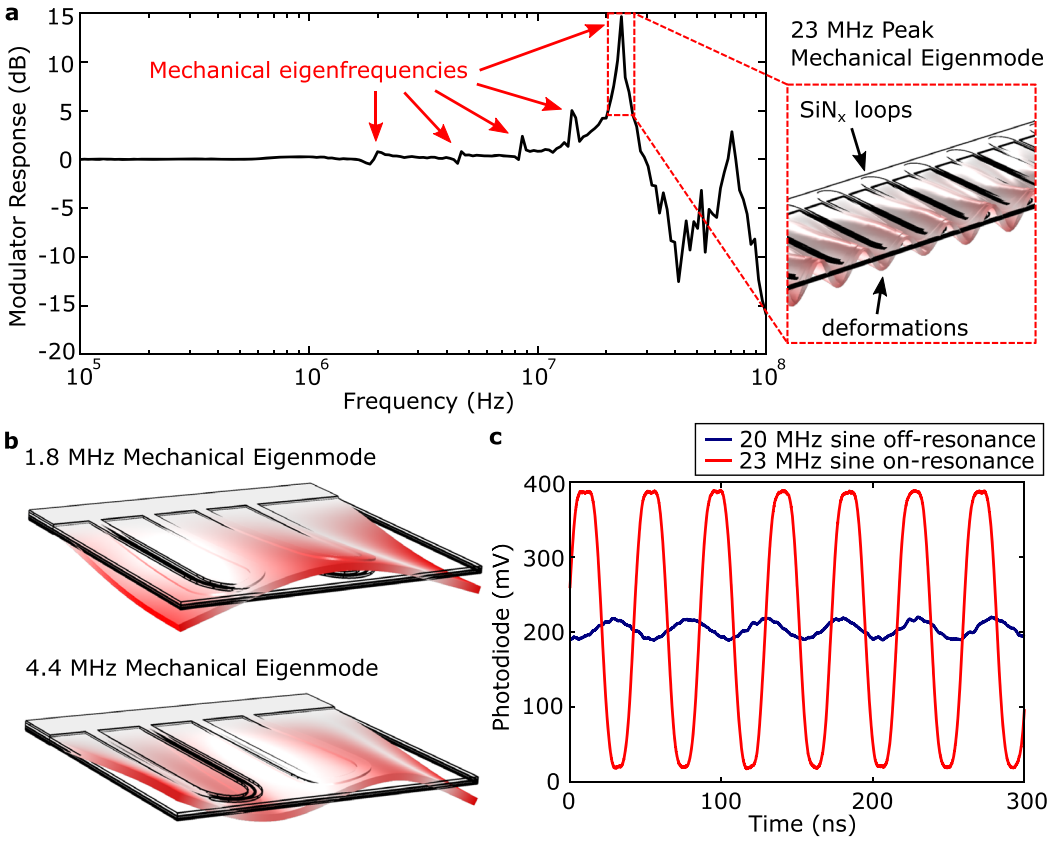

FIG. 5. Frequency response of a piezo-optomechanical modulator with design 2 parameters: (a) measured small-signal transfer function of the modulator, depicting several mechanical eigenfrequencies including a peak at 23 MHz highlighted with a 3D finite-element simulation of the eigenmode; (b) additional finite-element simulations of the second and third order mechanical eigenmodes at 1.8 and 4.4 MHz, respectively; (c) time trace of the modulator response driven with a 0.8 V pk–pk sinusoid at 20 MHz (off resonance) and 23 MHz (on resonance), showing a resonantly enhanced phase shift per volt.

overall suitability for large programmable photonic mesh circuits in the visible regime. The robustness of our fabrication process enables reliable cantilever performance and engineering of several important device parameters, including peak resonance frequency and V_π. We characterize additional cantilevers with varying overhang lengths from three different batches of wafers. Figures 6(a) and 6(b) show the measured single-loop V_π values at DC and peak cantilever resonance, respectively. Each data point is the average of three to five different cantilever modulators, with ±1 standard deviation error bars shown. Based on a least-squares fit, both the DC V_π and peak mechanical resonance f_R have a predictable inverse relationship with cantilever overhang, given by

$$V_\pi = a_V/(N_L h), \tag{3}$$

$$f_R = a_R/h, \tag{4}$$

where h is the cantilever overhang, N_L is the number of waveguide loops, and a_V and a_R are the slope coefficients of the V_π and peak resonance equations, respectively. We calculate a_V and a_R to be 42.7 V mm-loops and 1.81 MHz mm, respectively. From Eqs. (3) and (4), the critical parameters of V_π and f_R are quickly estimated by simply dividing a by the cantilever overhang and in the case of V_π, further divided by the number of waveguide loops. Unlike V_π, the peak mechanical resonance of the cantilever does not strongly depend on the number of waveguide loops. This behavior is explained by the resonance mode deformations [Fig. 5(b)], which is affected predominantly by the density of loops (nominally constant across all measured devices) over the cantilever area.

Despite the overall predictability of device performance, we see that the error bars in Fig. 6 increase as the cantilever overhang lengths get smaller. We attribute this effect to the smaller devices' increased sensitivity to fabrication variations. This uncertainty applies strongly to the V_π measurements and, to a lesser degree, the resonance frequency measurements. However, these MHz-range mechanical resonance frequencies maintain an uncertainty of less than one linewidth from the measured devices, making

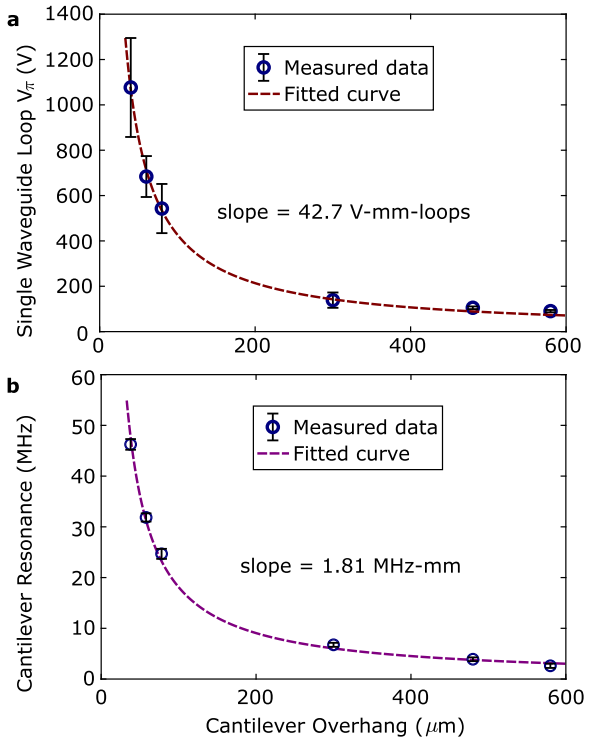

FIG. 6. Dependence of DC V_π and peak resonance frequency on cantilever overhang: (a) measured V_π values for various cantilevers with a fitted slope of a_V = 42.7 V mm-loops and (b) measured resonance frequency values for various cantilevers with a fitted slope of a_R = 1.81 MHz mm.

them more robust to fabrication variations compared to typical optical resonance structures.[39]

The broad ranges in operating voltage and bandwidth available to our cantilever modulator by simply adjusting parameters h and N_L allow for the engineering of larger photonic meshes to application-specific needs. Ultra-low-V_π MZMs are promising candidates for monolithically integrated photonics and CMOS electronic drivers[40]—a single-chip solution that allows for a small number of electronic inputs to control a large number of complex circuits. Optogenetics[41] and display technologies[42] would not require >1 MHz responses and would be well served by a larger cantilever with lower actuation voltage and power consumption. Other applications, such as optical switches and optical neural networks,[43] would benefit from shorter cantilevers with >10 MHz resonance frequencies for high-speed reconfiguration. Moreover, quantum network switches likely prefer modulators with shorter waveguides and low optical loss at the expense of higher drive voltages. Finally, driving multiple engineered cantilevers on-resonance would be beneficial for phased arrays and light ranging applications,[44,45] which require fast and cyclical control of many output beams.

SUPPLEMENTARY MATERIAL

See the supplementary material for additional device performance data.

ACKNOWLEDGMENTS

Major funding for this work was provided by MITRE for the Quantum Moonshot Program. D.E. acknowledges partial support from the DARPA ONISQ program, Brookhaven National Laboratory, supported by U.S. Department of Energy, Office of Basic Energy Sciences (Contract No. DE-SC0012704), and the NSF RAISE TAQS program. M.E. acknowledges partial support from the Center for Integrated Nanotechnologies, an Office of Science User Facility operated by the U.S. Department of Energy Office of Science. M.D. thanks Adrian Menssen, Ian Christen, and Artur Hermans for helpful technical discussions. M.D. also thanks Julia M. Boyle for characterizing the electrical impedances.

AUTHOR DECLARATIONS

Conflict of Interest

The authors have no conflicts to disclose.

DATA AVAILABILITY

The data that support the findings of this study are available from the corresponding authors upon reasonable request. The data are not publicly available.

REFERENCES

[1]W. Bogaerts, D. Pérez, J. Capmany, D. A. B. Miller, J. Poon, D. Englund, F. Morichetti, and A. Melloni, "Programmable photonic circuits," Nature **586**, 207–216 (2020).
[2]J. Capmany and D. Pérez, *Programmable Integrated Photonics* (Oxford, 2020), ISBN-10: 0198844409, ISBN-13: 978-0198844402.
[3]H. Choi, M. Pant, S. Guha, and D. Englund, "Percolation-based architecture for cluster state creation using photon-mediated entanglement between atomic memories," npj Quantum Inf. **5**, 104 (2019).
[4]H. Levine, A. Keesling, G. Semeghini, A. Omran, T. T. Wang, S. Ebadi, H. Bernien, M. Greiner, V. Vuletić, H. Pichler, and M. D. Lukin, "Parallel implementation of high-fidelity multiqubit gates with neutral atoms," Phys. Rev. Lett. **123**, 170503 (2019).
[5]M. Ruf, N. H. Wan, H. Choi, D. Englund, and R. Hanson, "Quantum networks based on color centers in diamond," J. Appl. Phys. **130**, 070901 (2021).
[6]S. Ebadi, T. T. Wang, H. Levine, A. Keesling, G. Semeghini, A. Omran, D. Bluvstein, R. Samajdar, H. Pichler, W. W. Ho, S. Choi, S. Sachdev, M. Greiner, V. Vuletić, and M. D. Lukin, "Quantum phases of matter on a 256-atom programmable quantum simulator," Nature **595**, 227–232 (2021).
[7]D. Kielpinski, C. Monroe, and D. J. Wineland, "Architecture for a large-scale ion-trap quantum computer," Nature **417**, 709–711 (2002).
[8]R. J. Niffenegger, J. Stuart, C. Sorace-Agaskar, D. Kharas, S. Bramhavar, C. D. Bruzewicz, W. Loh, R. T. Maxson, R. McConnell, D. Reens, G. N. West, J. M. Sage, and J. Chiaverini, "Integrated multi-wavelength control of an ion qubit," Nature **586**, 538–542 (2020).
[9]N. H. Wan, T.-J. Lu, K. C. Chen, M. P. Walsh, M. E. Trusheim, L. De Santis, E. A. Bersin, I. B. Harris, S. L. Mouradian, I. R. Christen, E. S. Bielejec, and D. Englund, "Large-scale integration of artificial atoms in hybrid photonic circuits," Nature **583**, 226–231 (2020).
[10]Y. Chen, A. Ryou, M. R. Friedfeld, T. Fryett, J. Whitehead, B. M. Cossairt, and A. Majumdar, "Deterministic positioning of colloidal quantum dots on silicon nitride nanobeam cavities," Nano Lett. **18**, 6404–6410 (2018).
[11]I. Aharonovich, D. Englund, and M. Toth, "Solid-state single-photon emitters," Nat. Photonics **10**, 631–641 (2016).
[12]C. D. Natale, "Chemical sensing benefits from simultaneous sensitivity to light and gases," Proc. SPIE (Published Online) (2014).

[13]D. A. B. Miller, "Analyzing and generating multimode optical fields using self-configuring networks," Optica **7**, 794 (2020).
[14]M. Reck, A. Zeilinger, H. J. Bernstein, and P. Bertani, "Experimental realization of any discrete unitary operator," Phys. Rev. Lett. **73**, 58–61 (1994).
[15]W. R. Clements, P. C. Humphreys, B. J. Metcalf, W. Steven Kolthammer, and I. A. Walsmley, "Optimal design for universal multiport interferometers," Optica **3**, 1460–1465 (2016).
[16]D. A. B. Miller, "Self-configuring universal linear optical component [Invited]," Photonics Res. **1**, 1–15 (2013).
[17]J. Carolan, C. Harrold, C. Sparrow, E. Martín-López, N. J. Russell, J. W. Silverstone, P. J. Shadbolt, N. Matsuda, M. Oguma, M. Itoh, G. D. Marshall, M. G. Thompson, J. C. F. Matthews, T. Hashimoto, J. L. O'Brien, and A. Laing, "Universal linear optics," Science **349**, 711–716 (2015).
[18]J. M. Arrazola, V. Bergholm, K. Brádler, T. R. Bromley, M. J. Collins, I. Dhand, A. Fumagalli, T. Gerrits, A. Goussev, L. G. Helt, J. Hundal, T. Isacsson, R. B. Israel, J. Izaac, S. Jahangiri, R. Janik, N. Killoran, S. P. Kumar, J. Lavoie, A. E. Lita, D. H. Mahler, M. Menotti, B. Morrison, S. W. Nam, L. Neuhaus, H. Y. Qi, N. Quesada, A. Repingon, K. K. Sabapathy, M. Schuld, D. Su, J. Swinarton, A. Száva, K. Tan, P. Tan, V. D. Vaidya, Z. Vernon, Z. Zabaneh, and Y. Zhang, "Quantum circuits with many photons on a programmable nanophotonic chip," Nature **591**, 54–60 (2021).
[19]N. C. Harris, G. R. Steinbrecher, M. Prabhu, Y. Lahini, J. Mower, D. Bunandar, C. Chen, F. N. C. Wong, T. Baehr-Jones, M. Hochberg, S. Lloyd, and D. Englund, "Quantum transport simulations in a programmable nanophotonic processor," Nat. Photonics **11**, 447–452 (2017).
[20]X. Qiang, X. Zhou, J. Wang, C. M. Wilkes, T. Loke, S. O'Gara, L. Kling, G. D. Marshall, R. Santagati, T. C. Ralph, J. B. Wang, J. L. O'Brien, M. G. Thompson, and J. C. F. Matthews, "Large-scale silicon quantum photonics implementing arbitrary two-qubit processing," Nat. Photonics **12**, 534–539 (2018).
[21]A. Ribeiro, A. Ruocco, L. Vanacker, and W. Bogaerts, "Demonstration of a 4 × 4-port universal linear circuit," Optica **3**, 1348–1357 (2016).
[22]T. Baehr-Jones, R. Ding, Y. Liu, A. Ayazi, T. Pinguet, N. C. Harris, M. Streshinsky, P. Lee, Y. Zhang, A. E.-J. Lim, T.-Y. Liow, S. H.-G. Teo, G.-Q. Lo, and M. Hochberg, "Ultralow drive voltage silicon traveling-wave modulator," Opt. Express **20**, 12014–12020 (2012).
[23]K. Alexander, J. P. George, J. Verbist, K. Neyts, B. Kuyken, D. Van Thourhout, and J. Beeckman, "Nanophotonic Pockels modulators on a silicon nitride platform," Nat. Commun. **9**, 3444 (2018).
[24]Y. Hu, M. Yu, D. Zhu, N. Sinclair, A. Shams-Ansari, L. Shao, J. Holzgrafe, E. Puma, M. Zhang, and M. Lončar, "On-chip electro-optic frequency shifters and beam splitters," Nature **599**, 587–593 (2021).
[25]F. Eltes, G. E. Villarreal-Garcia, D. Caimi, H. Siegwart, A. A. Gentile, A. Hart, P. Stark, G. D. Marshall, M. G. Thompson, J. Barreto, J. Fompeyrine, and S. Abel, "An integrated optical modulator operating at cryogenic temperatures," Nat. Mater. **19**, 1164–1168 (2020).
[26]C. Errando-Herranz, A. Y. Takabayashi, P. Edinger, H. Sattari, K. B. Gylfason, and N. Quack, "MEMS for photonic integrated circuits," IEEE J. Sel. Top. Quantum Electron. **26**, 8200916 (2020).
[27]C. Taballione, T. A. W. Wolterink, J. Lugani, A. Eckstein, B. A. Bell, R. Grootjans, I. Visscher, D. Geskus, C. G. H. Roeloffzen, J. J. Renema, I. A. Walmsley, P. W. H. Pinkse, and K.-J. Boller, "8 × 8 reconfigurable quantum photonic processor based on silicon nitride waveguides," Opt. Express **27**, 26842 (2019).
[28]A. Mohanty, Q. Li, M. A. Tadayon, S. P. Roberts, G. R. Bhatt, E. Shim, X. Ji, J. Cardenas, S. A. Miller, A. Kepecs, and M. Lipson, "Reconfigurable nanophotonic silicon probes for sub-millisecond deep-brain optical stimulation," Nat. Biomed. Eng. **4**, 223–231 (2020).
[29]Z. Yong, H. Chen, X. Luo, A. Govdeli, H. Chua, S. S. Azadeh, A. Stalmashonak, G.-Q. Lo, J. K. S. Poon, and W. D. Sacher, "Power-efficient silicon nitride thermo-optic phase shifters for visible light," Optics Express **30**, 7225–7237 (2022).
[30]B. Desiatov, A. Shams-Ansari, M. Zhang, C. Wang, and M. Lončar, "Ultra-low-loss integrated visible photonics using thin-film lithium niobate," Optica **6**, 380–384 (2019).
[31]M. Dong, G. Clark, A. J. Leenheer, M. Zimmermann, D. Dominguez, A. Menssen, D. Heim, G. Gilbert, D. Englund, and M. Eichenfield, "High-speed programmable photonic circuits in a cryogenically compatible, visible-NIR 200 mm CMOS architecture," Nat. Photonics **16**, 59 (2021).
[32]H. Tian, J. Liu, B. Dong, J. C. Skehan, M. Zervas, T. J. Kippenberg, and S. A. Bhave, "Hybrid integrated photonics using bulk acoustic resonators," Nat. Commun. **11**, 3073 (2020).
[33]D. A. B. Miller, "Perfect optics with imperfect components," Optica **2**, 747 (2015).
[34]P. R. Stanfield, A. J. Leenheer, C. P. Michael, R. Sims, and M. Eichenfield, "CMOS-compatible, piezo-optomechanically tunable photonics for visible wavelengths and cryogenic temperatures," Opt. Express **27**, 28588–28605 (2019).
[35]M. Huang, "Stress effects on the performance of optical waveguides," Int. J. Solids Struct. **40**, 1615–1632 (2003).
[36]D. Neculoiu, A.-C. Bunea, A. M. Dinescu, and L. A. Farhat, "Band pass filters based on GaN/Si lumped-element SAW resonators operating at frequencies above 5 GHz," IEEE Access **6**, 47587–47599 (2018).
[37]R. H. Olsson, K. Hattar, S. J. Homeijer, M. Wiwi, M. Eichenfield, D. W. Branch, M. S. Baker, J. Nguyen, B. Clark, T. Bauer, and T. A. Friedmann, "A high electromechanical coupling coefficient SH0 Lamb wave lithium niobate micromechanical resonator and a method for fabrication," Sens. Actuators, A **209**, 183–190 (2014).
[38]American National Standards Institute, *An American National Standard: IEEE Standard on Piezoelectricity Standard* (IEEE, 1988).
[39]W. Bogaerts, P. De Heyn, T. Van Vaerenbergh, K. De Vos, S. Kumar Selvaraja, T. Claes, P. Dumon, P. Bienstman, D. Van Thourhout, and R. Baets, "Silicon microring resonators," Laser Photonics Rev. **6**, 47–73 (2012).
[40]N. M. Fahrenkopf, C. McDonough, G. L. Leake, Z. Su, E. Timurdogan, and D. D. Coolbaugh, "The AIM photonics MPW: A highly accessible cutting edge technology for rapid prototyping of photonic integrated circuits," IEEE J. Sel. Top. Quantum Electron. **25**, 8201406 (2019).
[41]L. Hoffman, A. Subramanian, P. Helin, B. Du Bois, R. Baets, P. Van Dorpe, G. Gielen, R. Puers, and D. Braeken, "Low loss CMOS-compatible PECVD silicon nitride waveguides and grating couplers for blue light optogenetic applications," IEEE Photonics J. **8**, 2701211 (2016).
[42]M. Raval, A. Yaacobi, and M. R. Watts, "Integrated visible light phased array system for autostereoscopic image projection," Opt. Lett. **43**, 3678–3681 (2018).
[43]R. Hamerly, L. Bernstein, A. Sludds, M. Soljačić, and D. Englund, "Large-scale optical neural networks based on photoelectric multiplication," Phys. Rev. X **9**, 021032 (2019).
[44]J. Sun, E. Timurdogan, A. Yaacobi, E. S. Hosseini, and M. R. Watts, "Large-scale nanophotonic phased array," Nature **493**, 195–199 (2013).
[45]M. Chul Shin, A. Mohanty, K. Watson, G. R. Bhatt, C. T. Phare, S. A. Miller, M. Zadka, B. S. Lee, X. Ji, I. Datta, and M. Lipson, "Chip-scale blue light phased array," Opt. Lett. **45**, 1934–1937 (2020).